Superconducting Electromagnetic Launch System for Civil Aircraft

Luca Bertola, Tom Cox, Pat Wheeler, *Senior Member, IEEE*, Seamus Garvey, Herve Morvan

Abstract— **This paper considers the feasibility of different superconducting technologies for electromagnetic launch (EML) to assist civil aircraft take-off. EML has the potential of reducing the required runway length by increasing aircraft acceleration. Expensive airport extensions to face constant air traffic growth could be avoided by allowing large aircraft to operate from short runways at small airports. The new system positively affects total aircraft noise and exhaust emissions near airports and improves overall aircraft efficiency through reducing engine design constraints. Superconducting Linear Synchronous Motors (SCLSMs) can be exploited to deliver the required take-off thrust with electromagnetic performance that cannot be easily achieved by conventional electrical machines. The sizing procedure of a SCLSM able to launch A320 in weight is presented. Electromagnetic and thermal aspects of the machine are taken into account including the modelling of ac losses in superconductors and thermal insulation. The metallic high temperature superconductor (HTS) magnesium diboride (MgB_2) is used and operated at 20 K, the boiling temperature of liquid hydrogen. With modern manufacturing technology, multifilament MgB_2 wires appear to be the most cost-effective solution for this application. Finally the impact of the cryocooler efficiency on the machine performance is evaluated.**

Index Terms— **Biot-Savart law, civil aircraft, electromagnetic catapult, EML/EMLs, high temperature superconductor, linear synchronous motor, magnesium diboride, superconducting coil, superconducting linear accelerator.**

I. INTRODUCTION

ELECTROMAGNETIC Launch (EML) systems have been adopted to launch aircraft for military applications replacing steam catapults on the deck of aircraft carriers [1], [2]. This paper will describe the application of EML to propel civil aircraft on the runways of modern airports. The engine size of modern aircraft is principally determined by take-off conditions, since initial acceleration requires maximum engine

L. Bertola is with the Institute for Aerospace Technology, The University of Nottingham, NG7 2TU Nottingham, UK (e-mail: luca.bertola@nottinghma.ac.uk).

T. Cox and P. Wheeler are with the Electrical and Electronic Engineering Department, The University of Nottingham, NG7 2RD Nottingham, UK.

S. Garvey and H. Morvan are with the Department of Mechanical, Materials and Manufacturing Engineering, The University of Nottingham, NG7 2RD Nottingham, UK.
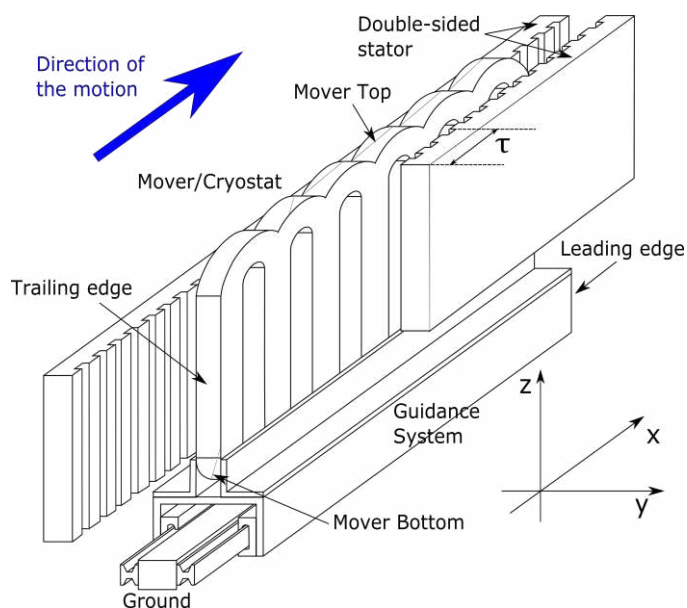

Fig. 1 Section of a double-sided SCLSM stator for a four-pole mover anchored to the guidance system

power. An EML system could provide some or all of the entire energy required at the launch stage so that the engine power requirement, on ground noise and fuel use and emissions may be significantly reduced. The thrust level that can be delivered by an EML system allows for accelerations that cannot be reached by aircraft engines. Consequently, EML systems have the potential of significantly reduce the nominal runway length required by the aircraft to take-off. Expensive airport extensions to face constant air traffic growth could be avoided by allowing large aircraft to operate from short runways at small airports.

It has already been shown in [3] and in [4] how conventional synchronous and asynchronous machines can be used to accelerate an A320 to the required take-off speed without the experience being uncomfortable for the passengers during take-off. Non-conventional HTS machines are recognized to offer some advantageous features like decrease in ac losses and consequent higher efficiency even accounting for cryocooler input power. To date, several Superconducting Linear Synchronous Motors (SCLSMs) that use bulk HTS on the machine's secondary have been proposed for military EML to produce the propulsion force [5], [6]. Existing SCLSMs with power requirements similar to those for civil EMLs employ superconducting coils to produce the required
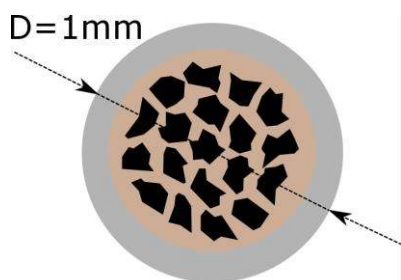
Fig. 2 Cross section of the MgB$_2$ wires from Columbus Superconductor [7]

field [8]. In a similar way the electromagnetic launcher proposed in this document has embedded superconducting coils (SCs) that produce the required propulsive force while a suspension force is not needed. The double-sided configuration has been selected to avoid the generation of normal forces. The track is placed vertically under the runway and is subdivided in sections which are progressively connected to the energy supply. Fig. 1 shows a cross section of the double-sided stator topology with an example of a guidance system connected a four-pole mover. The connection to the aircraft and the runway pavement were omitted for clarity, but they are position above the stator sides. Distributed stator windings were selected to limit the harmonic content of the magnetomotive force. The windings are fed at increasing frequency while the aircraft is moving. The SCs are made out MgB$_2$ wires for their low cost and simple manufacturing process. MgB$_2$ has a relatively low transition temperature (39 K) compared to other HTS, but the selected operating temperature of the mover (20 K) is very close to the temperature that should be used with YBCO or BSCCO-2223 tapes to get similar electromagnetic performance. So far, MgB$_2$ HTS has been employed to design a high-power rotary synchronous generator for wind turbine applications ([9], [10]), while this paper will exploit for EML systems.

The mover that is connected to the aircraft undercarriage (or main structure) is a cryostat which hosts the superconducting coils. Before each launch the cryostat is refilled with liquid hydrogen to keep the MgB$_2$ superconductors at the design temperature and sealed to avoid any hydrogen leakage. This cooling method has been selected to avoid any movable connection with the external refrigeration system and to reduce the number of machine components at cryogenic temperature. After the take-off speed is reached, the aircraft detaches and the mover is decelerated by a braking system. To prevent any additional thermal load, the mover slows down without any electromagnetic interaction with the superconducting coils using a mechanical brake, an external electromagnetic brake or a combination of both. The mover can be returned to the start position using the SCLSM while producing very little additional heating loss compared to the losses generated during launch. The machine stator operates at environmental temperature without any additional cooling. The mover structure is made out of aluminum for its low density and emissivity and for its high structural properties. The mover is ironless to reduce the weight and to avoid saturation of the ferromagnetic material.
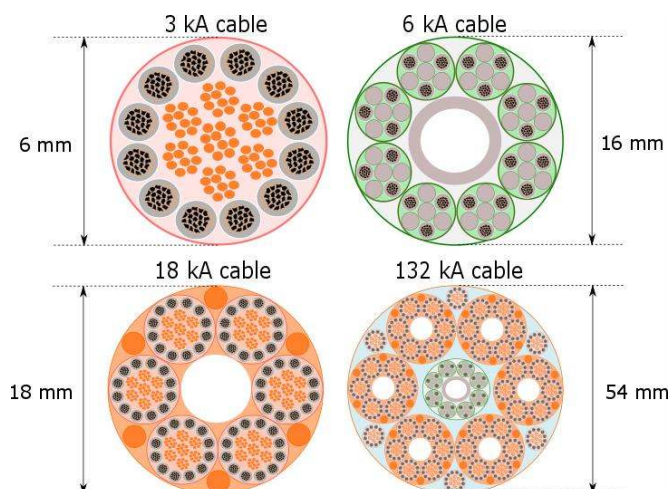

Fig. 3 Cross section of the superconducting cables used inside the moving cryostat. The currents refer to the max current density with a bias field of 2 T

In this paper, the sizing procedure of the SCLSM will be shown starting from the definition of the geometry of stator and superconductors to identification of the proper value of the insulation thickness to maintain the cryogenic temperature during the full launch. The procedure is meant to be general to be extended to any other superconducting synchronous motor.

II. SUPERCONDUCTOR GEOMETRY DEFINITION

The structure of the cables proposed for the superconducting launcher is very similar to the one adopted by CERN to achieve the world record in transport current in 2014 [11]. It is formed by MgB$_2$ wires from Columbus superconductor of 1 mm diameter whose section includes 19 superconducting filaments as shown in Fig. 2.

Considering the MgB$_2$ critical current density variation with the magnetic field, measured by CERN [11], the superconductor should be able to carry an electric current with a density of 1750 A/mm^2 when the external magnetic field density is 2 T (the average magnetic flux density that is expected to be in the middle of the mover during the launch).

With this field density the superconductor in Fig. 2 can carry a maximum current of approximately 250 A. Twelve of these wires can be wrapped around a copper core to form a cable that is capable of transferring 3 kA under 2 T, shown in Fig. 3. Copper is usually included to provide electrical and thermal protection for a superconducting wire in the unlikely event of a sudden loss of superconductivity due to exogenous factors. Six 3 kA cables are in turn wrapped around a cooling channel and embedded in a copper matrix to form an 18 kA cable as shown in Fig. 3. The cable on the top-right corner of the same figure is formed by 8 smaller cables that are twisted around a cooling channel and are able to carry 0.75 kA each. An epoxy membrane surrounds the 6 kA cable and each of the 0.75 kA cables that compose it. The final superconducting cable internal structure is an assembly of all the previous cables and should be able to transfer 132 kA when it is submerged in liquid hydrogen at 20 K. However, such a current would generate a magnetic field that would exceed the critical value of 2 T. To avoid local loss of superconductivity
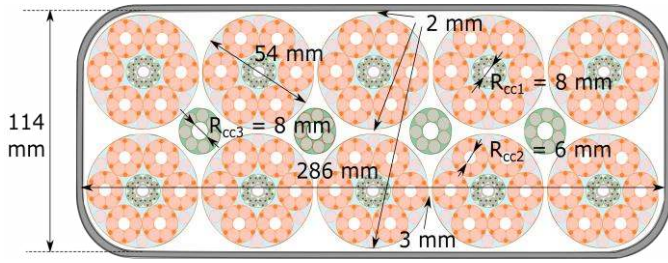
Fig. 4 Cross section of the cryostat with 10 superconducting cables and relative dimensions
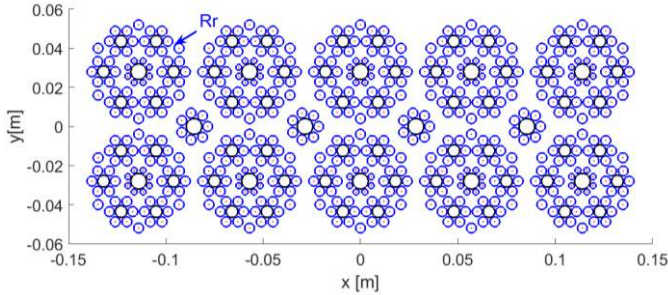

Fig. 5 Distribution of the superconducting rings for field approximated calculation
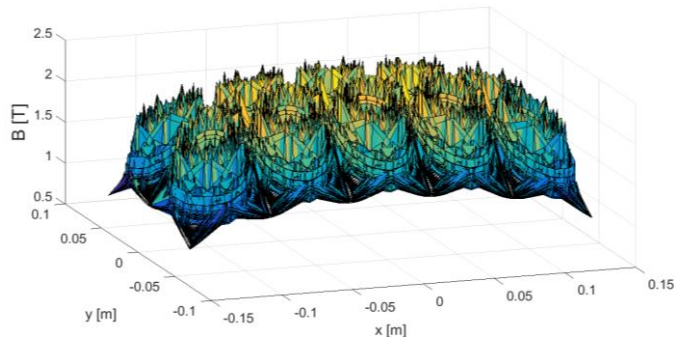

Fig. 6 3D view of the magnetic field density over the cryostat cross-section

and hot spots during the operating life the rated current density is set to a third of the critical value.

Under this assumption a single superconducting cable carries 44 kA. To achieve the magnetomotive force (MMF) intensity to produce the required thrust, 10 cables (N_1) were implemented. MMF of such intensity has been shown to be practically achievable in commercial magnetic levitation (MAGLEV) systems [8]. To reinforce the field strength some smaller cables (N_2), were inserted in the spaces available between the main ones to achieve the total MMF reported in Table II. These cables are formed by seven 3 kA cables wrapped around a cooling channel. The coils are tensioned and held in place by structural supports located inside the cryostat which have the role to withstand the load during launch operations. The coil section and the dimensions of the cryostat are shown in Fig. 4.

The magnetic field generated by the superconductors over the cryostat cross-section can be calculated approximating the 3 kA cables and the 0.75 kA cables as superconductive rings, shown in Fig. 5. The magnetic field B generated by a single ring can be computed using (1) for the area outside the ring and (2) for that inside.
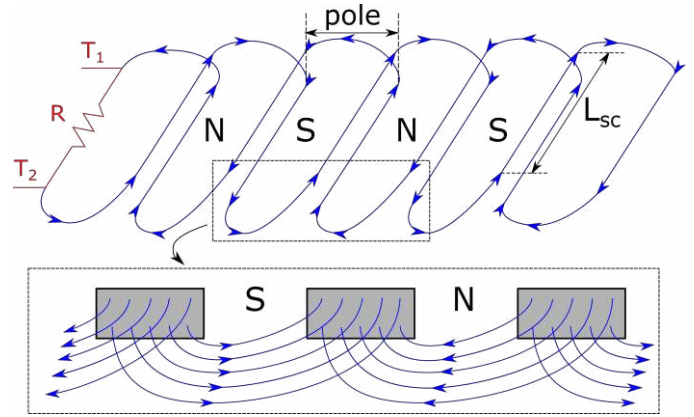

Fig. 7 Pattern followed by the bundle of superconducting cables inside the cryostat and end-coil configuration for a 4 poles SCLSM

$$B = \mu_0 I / (2\pi r) \tag{1}$$

$$B = \frac{\mu_0 I}{2\pi R_r} \tan \alpha_m \tag{2}$$

where I is rated current in the conductive ring; μ_0 is the permeability of the empty space; r is the vector distance; R_r is the radius of the rings; α_m is the twisting angle of the superconducting wires. The contributions of all the rings are than summed to get an approximation of the total field upon the cryostat section. A 3D view of the magnetic field is shown in Fig. 6. With a rated current density of 585 A/mm² the critical value of the magnetic field density is 4.8 T [11], while the max value of the magnetic field density generated by the superconductors at the center of the cryostat is approximately 2.3 T. Thus, this preliminary calculation proves that the superconductors do not quench under the combination of the rated current and magnetic field.

The N_1 turns are arranged in two layers and each turn of the top layer continues to the respective position of the bottom layer of the next cryostat section and vice versa for all the consecutive poles to form a pattern similar to the one in Fig. 7. The example in Fig. 7 shows the path of a superconducting cable for a four pole machine and the end-coil layout for 10 turns. The main superconducting cables are wound without crossovers and they proceed in parallel configuration across the cryostat sections without changing the cryostat thickness even over the end turns in Fig. 7. The five main 132-kA cables and two smaller 21-kA cables enter the cryostat at one end turn and are routed back and forth in parallel through the cryostat as shown in Fig. 7. After rounding the far end turn the cables double back through the cryostat so that each pole is surrounded by 10 cables as shown in Figs. 4 and 5, and exit from the first end turn near their starting point. The cryostat therefore has five closed superconducting loops, each one charged independently through a persistent-current switch whose resistor (R) and terminals T_1 and T_2 are reported in Fig. 7. The resistor presents no resistance at 20 K, while it is heated above the transition temperature during the SC ramping.

In general the cables on the outer side of the cryostat form loops that are longer than those on the inner side, although the
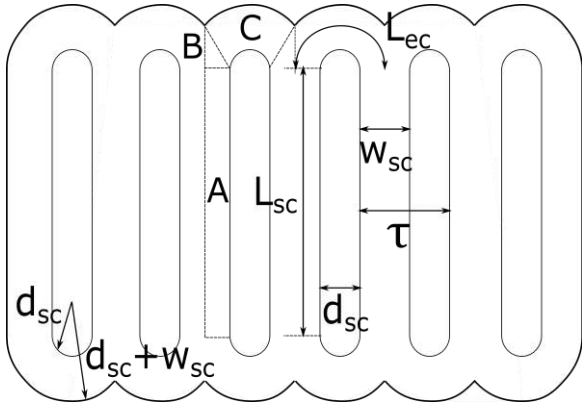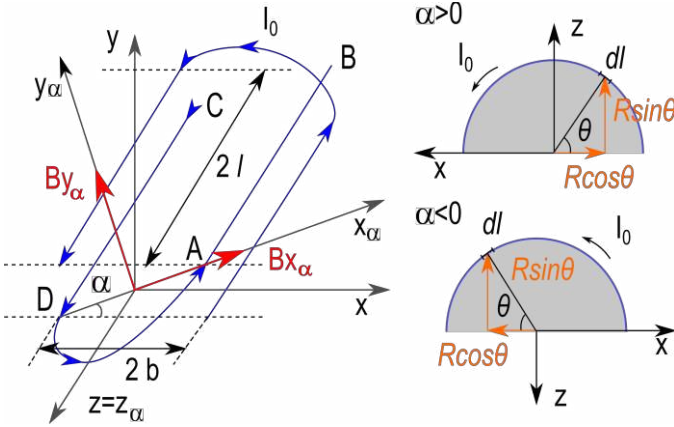
Fig. 8 Top view of the cryostat of a 4 poles SCLSM

Fig. 9 Machine and coil frames of reference considered for Biot-Savart integration
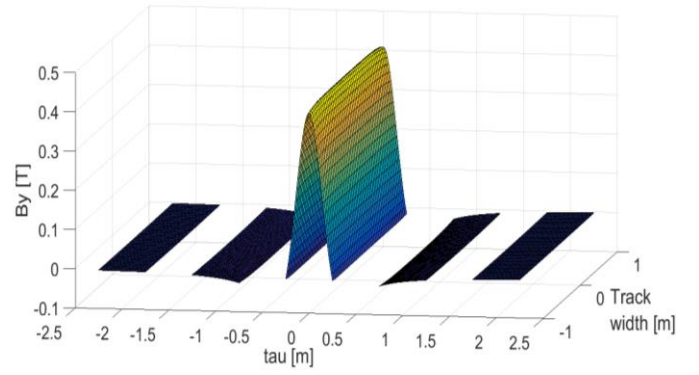

Fig. 10 Mean magnetic flux density generated by a superconducting pole over five neighbouring stator coils

volume of the main cables, while the second term that of the smaller cables. The numbers of cable sections N_1 and N_2 shown in Fig. 4 are halved in (6), since every cable of length L_{cable} doubles back on itself. In this way it covers two layers of the cryostat section as can be observed in Fig. 7. The volume of the liquid hydrogen that the cryostat can contain is given by (7) (see Table II).

$$V_{H2} = V_{cryo} - V_{cable} \qquad (7)$$

III. ELECTROMAGNETIC DESIGN

Once all the geometrical properties of the cryostat and of the superconducting cables are defined it is possible to apply the Biot-Savart law (8) to reconstruct the field generated by a single pole and then extend the results to the whole machine taking advantage of the symmetry of the magnetic wave.

$$\vec{B} = \frac{\mu_0 I}{4\pi} \int \frac{\vec{dl} \times \vec{r}}{r^3} \qquad (8)$$

Since the Biot-Savart law can be applied to current-carrying conductors with negligible thickness, the rings in Fig. 5 were approximated as cylindrical wires located on the respective centers. Considering the pattern followed by the wire shown in Fig. 7, the integration to calculate the field $\vec{B}$ generated by a single pole can be restricted to the evaluation of the contribution of U-loops in Fig. 9. Since the cryostat is aligned with the machine frame of reference shown in Fig. 1, the wire around a single pole must tilt with respect to the cryostat of an angle $\pm\alpha$ around the z-axis to pass from the bottom layer of the cryostat section in Fig. 5 to the top layer of the next cryostat section and vice versa. The tilt angle α reported in Fig. 9 changes for each U-loop according to the location of the superconducting ring in the cryostat section.

Since each U-loop lies on a plane, the integration of the Biot-Savart law can be applied to the wire in the tilted frame of reference in Fig. 9 to compute the magnetic field $\vec{B}_\alpha$. The integration is done separately for the straight parts and on the curved parts of the winding. While the integrals on the straight parts do not change between the top and bottom layers, the curved part switches position and current direction, and the integrand functions change accordingly. The field components generated by the wire in Fig. 9 on a generic point of coordinates x_P, y_P and z_P can be computed as shown in the

mean length of the cables can be computed as

$$L_{cable} = 2 \cdot (L_{sc} + L_{ec})(2p + 2) \qquad (3)$$

where L_{sc} is the stator stack width; L_{ec} is the end-coil length; p is the number of pole pairs. A top view of the cryostat for a four pole machine is shown in Fig. 8. The cryostat surface can be subdivided into simpler shapes (A, B and C in Fig. 8), that can be summed to calculate the total

area. Considering that the cryostat thickness h_{sc} is constant everywhere the total volume can be computed as

$$V_{cryo} = (2p + 2)(2V_A + 4V_B + 2V_C) + 2V_A + 4V_B. \qquad (4)$$

The terms of (4) can be expressed as shown in (5) by using the geometrical details highlighted in Fig. 8.

$$V_A = h_{sc}\frac{w_{sc}}{2}L_{sc}, \qquad V_B = \frac{\sqrt{3}}{8}h_{sc}w_{sc}{}^2,$$
$$V_C = \frac{\pi}{6}(w_{sc}{}^2 + 2d_{sc}w_{sc})h_{sc} \qquad (5)$$

The total volume occupied by the superconducting cables inside the cryostat is

$$V_{cable} = \pi\left(R_{cable}{}^2 - R_{cc1}{}^2 - 6R_{cc2}{}^2\right)L_{cable}\frac{N_1}{2}$$
$$+ \pi\left(R_{cable2}{}^2 - R_{cc3}{}^2\right)L_{cable}\frac{N_2}{2} \qquad (6)$$

where R_{cc1}, R_{cc2} and R_{cc3} are the radii of the cooling channels highlighted in Fig. 4. The first term of (6) represents the

Fig. 11 Schematic of the layered structure fo MLT applied to SCLSM

Fig. 12 Second order harmonic waveform over the stator slots and the airgap along a single pole pitch.

Appendix.

Equation (8) is integrated for each wire and then all the contributions are summed to calculate the magnetic field in the airgap and in the stator slots. Since the magnetic field density vector $\vec{B}_\alpha$ resulting from the integration of (8) is expressed in the tilted frame of reference, a coordinate transformation is required to find the magnetic field density $\vec{B}$ in the machine frame of reference (9).

$$
\begin{aligned}
B_x &= B_{x\alpha} \cos \alpha - B_{y\alpha} \sin \alpha \\
B_y &= B_{y\alpha} \sin \alpha + B_{y\alpha} \cos \alpha \\
B_z &= B_{z\alpha}
\end{aligned}
\tag{9}
$$

The optimal dimensions of the superconducting coil are determined by minimizing the difference between the calculated magnetic field waveform and the ideal sinusoidal wave and minimizing the volume of the cryostat.

In this procedure the pole pitch τ, stack width l_s and the airgap length g are determined. Considering the maximum operating frequency that commercial medium voltage power electronics can provide (approximately 250 Hz [12]) and considering the A320 take-off speed, the minimum pole pitch that can be selected is about 150 mm. However, the pole pitch length is determined by cryostat dimensions and bending radius of the superconducting cables (Fig. 8).

The stack width is a function of the maximum shear stress f_x that the cryostat can withstand. The value of the airgap length is a key parameter both for the electromagnetic and thermal design. The shorter the airgap length the greater is the magnetic flux that crosses the airgap and the lower is the current intensity to achieve the same thrust level. At the same time, the airgap hosts the superconducting magnets and the thermal insulation. The insulation has to keep the liquid hydrogen at its boiling temperature despite the heat flow coming from the external environment and the heat generated internally by the induced alternating current in the superconductors.

The airgap length is initially assumed, but the design algorithm must be iterated to find its optimum value. The magnetic flux component which interacts with the stator current to produce the thrust is the one that crosses the airgap perpendicularly along y-direction. The current is assumed to be uniformly distributed inside the slots while the magnetic flux density changes along the slot height h_s. Its average value can be computed as

$$
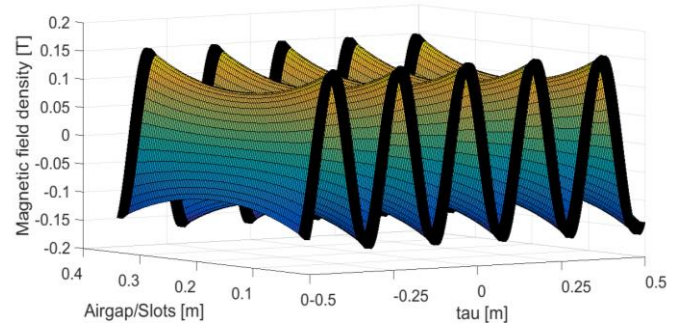\vec{B}_{y\,avg}(x,z) = \frac{1}{h_s} \int_0^{h_s} \vec{B}_y(x,y,z)\,dy.
\tag{10}
$$

By definition the magnetic flux across a surface is the integral of the magnetic flux density upon the same surface. Once the magnetic flux is obtained the stator rated current can be computed from

$$
I_s = \frac{2}{3} \frac{\tau}{\pi} \frac{F_x}{2\phi \cdot k_{w1} w_1}.
\tag{11}
$$

where 2ϕ is the magnetic flux produced by the two stators across the surface next to the mover, F_x is the thrust, k_{w1} is the winding factor, w_1 is the number of turns per phase and I_s is the current per turn. It has to be considered that the field generated by a single superconductor interacts also with neighbor track coils (Fig. 10), causing a braking effect due to the overall no-load voltage reduction and consequently, the current needed to produce the thrust increases. The current circulating in the stator coils generates a magnetic field whose fundamental harmonic is synchronized to the mover speed by the control system. The stator windings also generate a series of secondary harmonics with different intensities, synchronous speeds and frequencies. The superconducting coils "see" the secondary harmonics moving at a speed equal to difference between their synchronous speed and the fundamental one. The Multi-Layer Theory (MLT) is applied to reconstruct the field generated by the stator windings and its harmonic content [13]. The superconducting coils and the airgap are replaced by single layer having the permeability of air, while the slotted structure of stator is replaced by an anisotropic region where the permeabilities along x and y directions change. The final SCLSM schematic is represented in Fig. 11. An example of secondary harmonic waveform determined using MLT is shown in Fig. 12.

IV. LOSSES IN SUPERCONDUCTORS

During aircraft acceleration, the mover is synchronized with the fundamental electromagnetic wave in the airgap. Since the speeds of the secondary harmonics are different from the fundamental, they are unsynchronized with the motion. The alternating field of the secondary harmonics causes losses that can be classified as eddy current losses, hysteresis losses and coupling losses.

The travelling harmonic magnetic fields induce eddy currents which mainly flow in radial direction in the superconductor's matrix. An analytical formula to calculate the losses in the matrix due to the sinusoidally time-varying
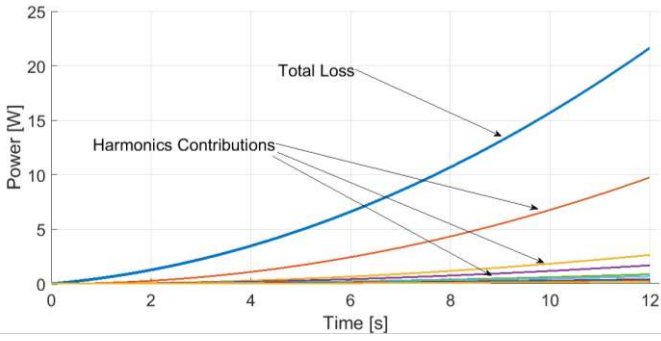
Fig. 13 Eddy currents losses variation during aircraft acceleration

Fig. 15 Coupling losses variation during aircraft acceleration

inside the superconductor. The superconducting material has then microscopic domains of normal state, through which a magnetic flux passes forming a pinned structure that remains even if external forces like magnetic field or transport current are removed. This hysteresis phenomenon can be simply described by the Maxwell equations in the Bean approximation in the limit cases of full penetration and weak penetration [16]. Intermediate conditions will be treated by approximation. When a wire is carrying a fixed dc current with an external alternating transverse field that leads to full penetration the solution of the Maxwell equations gives a power loss per unit volume

$$\frac{P}{V} = \frac{4}{3\pi} \mu_0 j_c r_w |\dot{H}| g\left(\frac{I}{I_c}\right) \tag{13}$$

where the function $g(x)$ and the ratio between the transport current and the critical current I/I_c can be computed with (14) and (15) respectively.

$$g(x) = \left(1 - \frac{y_1^2}{r_w^2}\right)^{3/2} + \frac{3\pi}{4}\frac{|y_1 x|}{r_w} \tag{14}$$

$$\frac{I}{I_c} = \frac{2}{\pi}\left(\frac{y_1}{r_w}\sqrt{1 - \frac{y_1^2}{r_w^2}} + \sin^{-1}\frac{y_1}{r_w}\right) \tag{15}$$

where j_c is the critical current density, $|\dot{H}| = \omega H_0$ is the amplitude of the derivative of the magnetic field and y_1 is the inner coordinate where the fully penetrated field changes sign. In case of weak penetration the losses per volume are

$$\frac{P}{V} = \frac{128}{9\pi}\mu_0 \frac{H_0^3}{r_w j_c} \tag{16}$$

To extend these formulas to the case of partial penetration an analytic approximation proposed in [16] and based on the interpolation of (13) and (16) is shown in (17).

$$P = \frac{8}{3}\frac{(f - f_v)\frac{l_{cable}}{2}\pi r_w^2 \frac{B_p^2}{\mu_0}\left(\frac{B_w}{B_p}\right)^3}{\frac{3\pi^2}{32} + \left(\frac{B_w}{B_p}\right)^2} g\left(\frac{I}{I_c}\right) \tag{17}$$

where $B_p = 2\mu_0 r_w j_c (1 - I/I_c)/\pi$ is the penetration field. The hysteresis losses linear variation with time, calculated with (17), is shown in Fig. 14.

The coupling losses of the superconducting cables are determined considering the matrix from the voltage equation (18) for a bundle of wires.
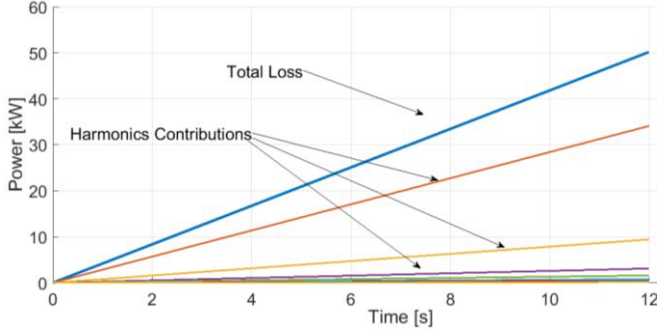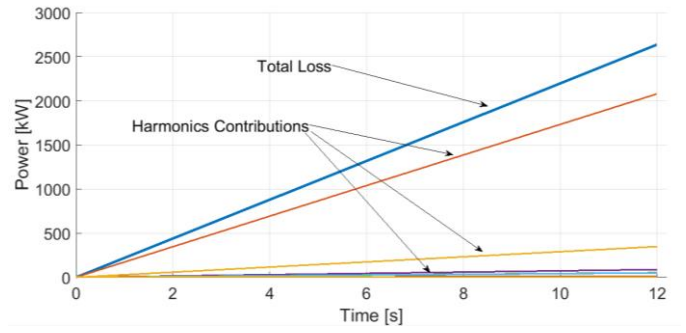

Fig. 14 Hysteresis losses variation during aircraft acceleration

external magnetic field that is perpendicular to the wire's axis has been proposed in [14]. It is rewritten here to estimate the eddy current losses P_{eddy} (in W), as a function of the twist pitch angle α_m (12).

$$P_{eddy} = 2B_w^2 \frac{f^2 \rho_m \pi^3 r_w^4 (\tan\alpha_m)^2}{f^2 \mu_0^2 \pi^2 r_w^4 (\tan\alpha_m)^4 + \rho_m^2} L_{cable} \tag{12}$$

where B_w is the magnetic field amplitude in each wire, f the relative frequency, ρ_m is the resistivity of the matrix, r_w is the radius of the wire (equal to $D/2$ in Fig. 1) and L_{cable} is the length of the superconducting cable.

Since the first term at the denominator in (12) is negligible with respect to ρ_m^2, P_{eddy} can be considered inversely proportional to the matrix resistivity. In (12), ρ_m should be replaced by the effective transverse resistivity ρ_{et} which can be much smaller than ρ_m and takes into account the MgB$_2$ filaments distribution over the wire's cross section. Even though resistivity is a key parameter for eddy current losses calculation, P_{eddy} is so small compared to the other sources of loss that the efforts to accurately compute ρ_{et} are not strictly required.

Therefore the results plotted in Fig. 13 should be considered as an approximation. The chart shows the total eddy current loss together with the contributions of the first nine harmonics. Eddy currents are also induced in the hydrogen vessel and in the aluminum structure of the cryostat. As it has been proved in [15], the losses on the aluminum vessels are negligible (below 1 W per pole), but they were considered for analysis completeness of the analysis.

Type-II superconductors like MgB$_2$ normally operate above the first critical magnetic field H_{c1} under the condition called mixed state where the magnetic field partially penetrates
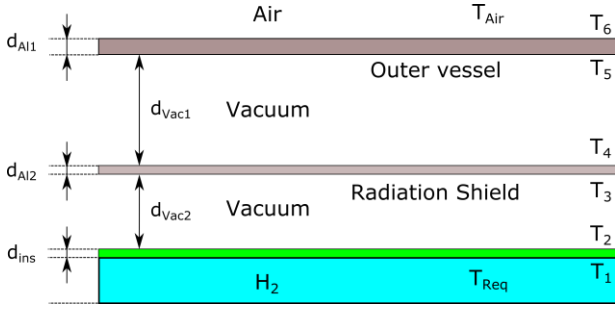
Fig. 16 Schematic of the layered structure of the thermal insulation used for the 1D heat transfer model

$$\begin{bmatrix} V_1 \\ V_2 \\ \vdots \\ V_n \end{bmatrix} = \begin{bmatrix} j\omega L_1 + R_1 & M_{12} & \cdots & M_{1n} \\ M_{21} & j\omega L_2 + R_2 & \cdots & M_{2n} \\ \vdots & \vdots & \ddots & \vdots \\ M_{n1} & M_{n2} & \cdots & j\omega L_n + R_n \end{bmatrix} \begin{bmatrix} I_1 \\ I_2 \\ \vdots \\ I_n \end{bmatrix} \quad (18)$$

The mutual inductances of the wires wrapped around a central core to form a "3 kA cable" and a "750 A cable" (Fig. 3) are computed solving the Neumann integral (19) for two helical filaments. Applying the principle of geometric mean distance, the same integral can be solved for a finite conductor to calculate the self-inductance [17].

$$M_{ij} = \frac{\mu_0}{4\pi} \oint \oint \frac{ds_i \cdot ds_j}{R} \quad (19)$$

For the wires that do not belong to the same aforementioned cables the mutual inductance is approximated using the formula for two parallel filaments of length l and distance d [18].

$$M_{ij} = \frac{\mu_0}{2\pi} \left(l \cdot log \frac{l + \sqrt{l^2 + d_{ij}^2}}{d_{ij}} - \sqrt{l^2 + d_{ij}^2} + d_{ij} \right) \quad (20)$$

Once (18) is solved the coupling loss can be simply computed using $P = V \cdot I$. The variation of the coupling losses with time is shown in Fig. 15.

V. THERMAL INSULATION

The thermal insulation system that is proposed for SCLSM is similar to the one adopted for MAGLEV trains [19]. The superconducting coils are hosted inside an isolated inner vessel separated by a radiation shield from the outer vessel. The space between the outer and inner vessels is evacuated to allow only radiation heat to be exchanged. Conduction occurs only through the sustaining structure, but it can be limited with an accurate thermal design. In MAGLEV applications to further reduce the heat flow across the insulation the radiation shield is cooled down using liquid nitrogen. However, since MgB$_2$ replaces the niobium-tin superconductors, the operative temperature rises from 4.2 K to 20 K, and there is no need to cool the radiation shield. Liquid hydrogen has been chosen as main coolant to exploit its excellent thermal properties, specifically its high evaporation latent heat.

The one-dimensional heat transfer model schematizes the mover structure with layers of different materials as shown in Fig. 16. The thermal insulation model first solves the static
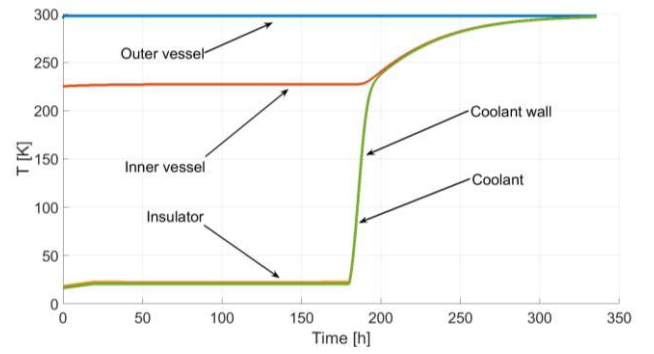

Fig. 17 Temperature distribution on the insulation's layered structure with convective heat transfer and no internal heat generation.
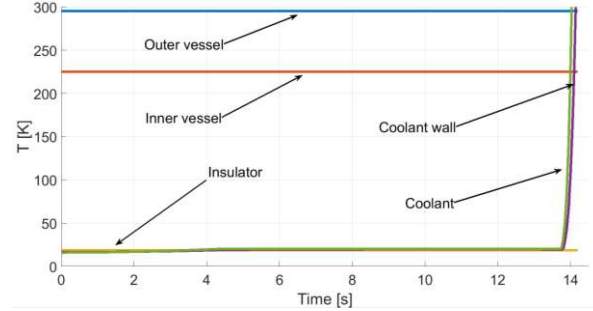

Fig. 18 Temperature distribution on the insulation's layered structure with internal generation

heat transfer problem to obtain the temperature distribution along the mover thickness which is used as initial condition for the transient heat transfer problem. This method represents what happens in the real application: between two launches the mover is connected to the cryocooler and the system is cooled down to the desired temperatures (calculated by the static model), and immediately afterward the launch procedure begins (simulated by the transient model). The one-dimensional model neglects the conduction heat that flows through the support structure and the heat that is transferred across the mover leading edge, trailing edge, bottom surface and top surface (see Fig. 1). These contributions are marginal with respect the total heat that flows across the lateral surfaces and the heat that is generated internally.

The total thickness of the structure under study is equal to the airgap length that has been considered for the electromagnetic design. While most of the mover dimensions, surfaces and volumes are computed by the ac losses tool, the thickness of the various layers has to be defined. In [3] it has been proved that an aluminum slab with 20 mm of thickness is able to withstand the max propulsion force without buckling instability. Therefore, it is reasonable to assume that the sum of the thicknesses of the aluminum layers has to be greater than this value. One might object that splitting the total thickness defined in [3] in more layers should make the structure intrinsically more unstable under the same axial load. However, in SCLSM the aluminum layers are connected by several supports which constraint the layers displacement and help to prevent the buckling instability. To be conservative, the total aluminum thickness is assumed to be 30 mm.

The performance of the insulation was first analyzed without ac losses and only later the internal heat generation

TABLE I
LIST OF REQUIREMENTS FOR THE A320 LAUNCHER

Requirements	A320 Launch
Aircraft mass	73500 kg
Take-off speed	70.63 m/s
Acceleration	0.60 G
Peak Thrust	548 kN
Runway length	535 m
Take-off time	12 s
Minimum cycle time	90 s

TABLE II
SCLSM PARAMETERS

Name	Value	Name	Value
Pole pitch	0.500 m	Cryostat thickness	0.114 m
Slot pitch	0.167 m	Cryostat Volume	1.234 m^3
Slot height	0.020 m	Hydrogen Volume	0.570 m^3
Stator width	2.000 m	Cables Volume	0.664 m^3
Pole pairs	4	MgB$_2$ Volume	0.0256 m^3
Number of phase	3	SC cable length	60.997 m
Turns per slot	6	MMF	468 kA turns
Mover length	5.00 m	Thrust density	55 kN/m^2
Mover height	2.602 m	Stator resistance	0.120 Ω
Mover surface	13.01 m^2	Stator inductance	0.425 mH
Cryostat surface	10.82 m^2	Max frequency	71 Hz

was introduced. In the former case the convective coefficient of air increases only during the take-off time (the first 12 s), and then it remains constant and equal to the last value of the loaded data until the end of the simulation. Fig. 17 shows the temperature variation of the layers with time. It can be clearly seen that when hydrogen is boiling, the temperature distribution of the system does not change until all the hydrogen evaporates. This happens after 180 hours (about 7 days), because the amount of hydrogen stored inside the mover is able to absorb 18.73 MJ before changing phase completely, and the heat that flows across the insulation is only 37.5 W. After the hydrogen evaporation the system tends to the temperature of the air.

Including the ac losses the liquid hydrogen does not reach the vaporization before the end of the acceleration. With heat generation the hydrogen would fully evaporate after 13.8 s (which is longer that the take-off time) as shown in Fig. 18. Since launch heat generation ceases after 12 s, the heat flow across the insulation would cause the full hydrogen evaporation after approximately 19 hours. However, the mover needs to return to its initial position and must be capable of absorbing the additional ac losses produced in the process. Assuming that the mover returns in 30 seconds with an uniformly accelerated motion (constant force for simplicity), and that the SCLSM efficiency is constant, the additional ac losses can be approximated as

$$Q_{AC} = E_{mov} \frac{Q_{LH2}}{E_{A320}} \tag{21}$$

where E_{mov} is the energy transferred to the mover during the return phase, Q_{LH2} is the energy absorbed by the liquid hydrogen during the launch (total ac losses) and E_{A320} is the energy transferred to the aircraft and the mover during the launch. Considering the additional heating Q_{AC} the time window for post-launch operations before full hydrogen evaporation is approximately 17 hours.

VI. MACHINE PERFORMANCE INCLUDING CRYOCOOLER EFFICIENCY

The electromagnetic and thermal design procedure described in this paper has been applied to a SCLSM to fulfil the requirements reported in Table I.

The final airgap length of the machine is the result of an iterative procedure which optimizes thermal and electromagnetic performances. In this process all the other

features of the motor were kept constants (Table II). Since the armature MMF is notably smaller than that of the superconducting coils the leakage stator inductance per phase L_s in Table II may be calculated as for long electric power lines including the influence of the other two phases [20]. This allows for the calculation of the reactive power Q_1 as

$$Q_1 = 3 \, \omega \, L_s I_s^2 \tag{22}$$

where ω is the input frequency and I_s is the stator current. Table III shows the design outcomes for two different airgap lengths including the effect of the cryocooler input power on the machine performances. The cryogenic refrigeration system under consideration is a Reverse-Brayton cryocooler (RBC) for aerospace application which has been proposed for future distributed propulsion aircraft architecture [21]. The required cooling power Q_c has been computed as

$$Q_c = P_{AC} t_{to}/(2t_c), \tag{23}$$

where P_{AC} is the peak alternating current loss, 2 comes from the integration of the ac losses as linearly increasing function, t_{to} is the take-off time and t_c is the minimum time between two consecutive launches (cycle time in Table I). Hydrogen absorbs energy only during the take-off while the cryocooler needs to be capable of removing the same amount of heat in t_c seconds. Table III reports the input powers of the cryocooler with liquid nitrogen (LN$_2$) or water at the heat sink. In the former case it has an efficiency of 5.52% (36.97% of Carnot efficiency), while it has an efficiency of 1.35% (38.24% of Carnot efficiency) with water.

According to the structure of the design procedure, the length of the mover and the number of poles are calculated from the thrust density in input. Therefore the value of the thrust density is determined through an iterative procedure which takes into account structural, electromagnetic and thermal aspects of the machine.

Since the stator current I_s linearly increases with the thrust density while the input power slightly changes, the voltage exponentially decreases. The line voltage reported in Table III can be handled using multi-level inverters which break down the voltage to a level that allows the power semiconductor devices to operate [12]. Since the total ac losses increases with

TABLE III
SCLSM PERFORMANCE WITH DIFFERENT AIRGAPS

Name	g = 15 cm	g = 10 cm
Peak airgap magnetic field density	1.254 T	1.445 T
Average armature field density	0.798 T	1.060 T
Rated current per turn (RMS)	1277 A	965.5 A
Peak Voltage	10964 V	14813V
Rated slot current density	22.29 A/mm^2	16.86 A/mm^2
Peak active power	41.985 MW	42.922 MW
Peak reactive power	0.922 MW	0.528 MW
Peak efficiency	0.9220	0.9999
Power factor	0.9998	1.0000
Peak efficiency with LN_2-LH_2 cryocooler	0.8498	0.8053
LN_2-LH_2 crycooler input power	3.570 MW	5.148 MW
Peak efficiency with H_2O-LH_2 cryocooler	0.6842	0.6051
H_2O-LH_2 crycooler input power	14.596 MW	21.050 MW
LH_2 boiling time	13.8 s	12.1 s
Addition LH_2 volume	1.313 m^3	2.398 m^3
Mover mass	7092 kg	6996 kg

the thrust density while the volume of the cryostat decreases, an additional tank of liquid hydrogen is needed to give efficient cooling. The additional volume of the liquid hydrogen is determined to have evaporation of a maximum the 20% of the total coolant mass (Table III). The weight of coolant in excess does not represent an additional design constraint since the density of liquid hydrogen is very low. Moreover, a tank would be required to regulate the pressure changes due to the hydrogen evaporation.

The thermal model presented in this paper assumes forced convection on the air side and natural convection on the liquid hydrogen side (Fig. 16). The amount of heat removed by the SCs will be increased by continuous flow along the narrow ducts of the cryostat forced by a pump located in the hydrogen tank. The pump would grant a homogeneous temperature distribution and would prevent the superconductors quenching during operations.

VII. CONCLUSION

A design procedure for superconducting EML systems has been proposed for an A320 or similar sized civil aircraft. The actual MgB_2 manufacturing technology readiness has been proved suitable for this demanding application. In particular the good mechanical properties, low bending radius, round cable availability and no need for texturing are advantages that can be exploited in superconducting EML launchers. With the continuous developments in MgB_2 doping processes, current density improvements under high external magnetic field can be envisaged. Other HTSs, like second generation YBCO

wires, may become interesting for EML when future developments will make them more affordable. Below the boiling temperature of liquid nitrogen, liquid hydrogen is the best coolant that can be employed due to the high latent heat that is exchanged during evaporation. At hydrogen's change of phase temperature, MgB_2 wires are the most cost-effective solution being approximately 20 times less expensive than YBCO tapes [9].

The major power loss inside the superconductors is due to the inductive coupling between MgB_2 wires. In this paper the calculation of mutual and self inductances does not take into account any magnetic shielding produced either by the wire matrix or by the cryostat structure, so the final ac losses of the SCLSM are expected to be lower. Even with high levels of loss, the cooling system is able to cope with the internal heat generation maintaining 20 K during the duration of the launch. While, the cooling power requirement for the cryocooler remains considerably large, it can be fulfilled by the single RBC proposed in this paper or by multiple smaller cryocoolers which add direct and operating costs to the system.

The structural integrity of the mover is given by the conservative assumptions made on the aluminum layers thickness and on the thrust density. Nevertheless, structural analysis should be carried out to optimize the thickness distribution and then reduce the mover weight. The thrust density is a key parameter to determine because it affects the electromagnetic performance of the machine. However the complexity of the mover structure and uncertainty due to lack of an experimental set up, motivate the cautious assumptions made during the preliminary design while waiting for future validations.

When compared with linear induction machines and permanent magnet synchronous machines for EML [4], the superconducting motor presents outstanding electromagnetic performance especially when it is evaluated as an isolated system. However, when the cryocooler input power is considered to estimate the efficiency, the performances of the overall system are comparable with those achievable with conventional technologies that operate at environmental temperature. The weight of the SCLSM mover in Table III is almost equivalent to the 10% of the A320's weight, so that a significant portion of the energy delivered by the system is transferred to the mover rather than to the aircraft. The complexity of the system and the cost of the cooling remain significant challenges to be overcome in the implementation of superconducting EML systems. However, when the costs of runway extension (£12 billion [22]) or runway construction (£18.6 billion [23]) to face air traffic growth are considered, the installation of the electromagnetic catapult becomes an economically viable solution.

APPENDIX

The field components generated by filament AB (Fig. 9), in a generic point of coordinates x_P, y_P and z_P can be computed as illustrated by (24). The calculation is made on the tilted frame of reference in Fig. 9, but the formulation is general.

$$\vec{dl}_{AB} = [0 \quad 0 \quad -dz_\alpha], \qquad \vec{r}_{AB} = [x_P - b \quad y_P \quad z_P - z_\alpha] \qquad (24)$$

$$\overrightarrow{dl}_{AB} \times \vec{r}_{AB} = y_P dz_\alpha \,\vec{\imath} - (x_P - b)\vec{\jmath}$$

$$\vec{B}_{\alpha\,AB} = [B_{\alpha x\,AB} \quad B_{\alpha y\,AB} \quad 0] = \frac{\mu_0 I}{4\pi} \int_{-l}^{l} \frac{y_P dz_\alpha \,\vec{\imath} - (x_P - b)\vec{\jmath}}{\left[(x_P - b)^2 + y_P^2 + (z_P - z)^2\right]^{3/2}} dz_\alpha$$

$$B_{\alpha x\,AB} = \frac{\mu_0 I}{4\pi} \cdot \frac{y_P}{(x_P - b)^2 + y_P^2} \left[\frac{l - z_P}{\sqrt{(x_P - b)^2 + y_P^2 + (z_P - l)^2}} + \frac{l + z_P}{\sqrt{(x_P - b)^2 + y_P^2 + (z_P + l)^2}} \right]$$

$$B_{\alpha y\,AB} = \frac{\mu_0 I}{4\pi} \cdot \frac{x_P - b}{(x_P - b)^2 + y_P^2} \left[\frac{z_P - l}{\sqrt{(x_P - b)^2 + y_P^2 + (z_P - l)^2}} - \frac{l + z_P}{\sqrt{(x_P - b)^2 + y_P^2 + (z_P + l)^2}} \right]$$

In a similar way the field components generated by filament CD can be computed using (25).

$$B_{\alpha x\,CD} = \frac{\mu_0 I}{4\pi} \cdot \frac{y_P}{(x_P + b)^2 + y_P^2} \left[\frac{z_P - l}{\sqrt{(x_P - b)^2 + y_P^2 + (z_P - l)^2}} - \frac{l + z_P}{\sqrt{(x_P - b)^2 + y_P^2 + (z_P + l)^2}} \right]$$

$$B_{\alpha y\,CD} = \frac{\mu_0 I}{4\pi} \cdot \frac{x_P + b}{(x_P + b)^2 + y_P^2} \left[\frac{l - z_P}{\sqrt{(x_P - b)^2 + y_P^2 + (z_P - l)^2}} + \frac{l + z_P}{\sqrt{(x_P - b)^2 + y_P^2 + (z_P + l)^2}} \right] \tag{25}$$

For the curved filament the integrand functions change with the sign of the angle α in Fig. 9. In case $\alpha > 0$ the magnetic field components are computed as in (26) while when $\alpha < 0$ they are calculated using (27).

$$\overrightarrow{dl} = [Rd\theta \sin\theta \quad 0 \quad Rd\theta \cos\theta], \qquad \vec{r}_{AB} = [x_P + R\cos\theta \quad y_P \quad z_P - l - R\sin\theta]$$

$$\overrightarrow{dl}_{AB} \times \vec{r}_{AB} = -y_P Rd\theta \cos\theta \,\vec{\imath} + [R\cos\theta\,(x_P + R\cos\theta) - R\sin\theta\,(z_P - l - R\sin\theta)]\vec{\jmath} + y_P Rd\theta \sin\theta \,\vec{k}$$

$$B_{\alpha x} = \frac{\mu_0 I}{4\pi} \cdot \int_0^\pi \frac{-y_P R\cos\theta}{\left[(x_P + R\cos\theta)^2 + y_P^2 + (z_P - l - R\sin\theta)^2\right]^{3/2}} d\theta$$

$$B_{\alpha y} = \frac{\mu_0 I}{4\pi} \cdot \int_0^\pi \frac{R\cos\theta\,(x_P + R\cos\theta) - R\sin\theta\,(z_P - l - R\sin\theta)}{\left[(x_P + R\cos\theta)^2 + y_P^2 + (z_P - l - R\sin\theta)^2\right]^{3/2}} d\theta \tag{26}$$

$$B_{\alpha z} = \frac{\mu_0 I}{4\pi} \cdot \int_0^\pi \frac{y_P R\sin\theta}{\left[(x_P + R\cos\theta)^2 + y_P^2 + (z_P - l - R\sin\theta)^2\right]^{3/2}} d\theta$$

When integrating for $\alpha < 0$ keep in mind that θ reverses so $\cos\theta$ changes sign.

$$\overrightarrow{dl} = [-Rd\theta \sin\theta \quad 0 \quad Rd\theta \cos\theta], \qquad \vec{r}_{AB} = [x_P + R\cos\theta \quad y_P \quad z_P + l + R\sin\theta]$$

$$\overrightarrow{dl}_{AB} \times \vec{r}_{AB} = -y_P Rd\theta \cos\theta \,\vec{\imath} + [R\cos\theta\,(x_P + R\cos\theta) + R\sin\theta\,(z_P + l + R\sin\theta)]\vec{\jmath} - y_P Rd\theta \sin\theta \,\vec{k}$$

$$B_{\alpha x} = \frac{\mu_0 I}{4\pi} \cdot \int_0^\pi \frac{-y_P R\cos\theta}{\left[(x_P + R\cos\theta)^2 + y_P^2 + (z_P + l + R\sin\theta)^2\right]^{3/2}} d\theta$$

$$B_{\alpha y} = \frac{\mu_0 I}{4\pi} \cdot \int_0^\pi \frac{R\cos\theta\,(x_P + R\cos\theta) + R\sin\theta\,(z_P + l + R\sin\theta)}{\left[(x_P + R\cos\theta)^2 + y_P^2 + (z_P + l + R\sin\theta)^2\right]^{3/2}} d\theta \tag{27}$$

$$B_{\alpha z} = \frac{\mu_0 I}{4\pi} \cdot \int_0^\pi \frac{-y_P R\sin\theta}{\left[(x_P + R\cos\theta)^2 + y_P^2 + (z_P + l + R\sin\theta)^2\right]^{3/2}} d\theta$$

The field components in (26) and in (27) were computed numerically because the integrals could not be written in closed form like for straight wires.

REFERENCES

[1] K. Lentijo, G. Bellamy, J. Watson, K. Flint, "Launch and Recovery using the EMKIT System," ed: Amercian Society of Naval Engineer 2010.
[2] G. Atomics. (2014, October). *EMALS*. Available: http://www.ga.com/emals
[3] L. Bertola, T. Cox, P. Wheeler, S. Garvey, H. Morvan, "Civil Application of Electromagnetic Aircraft Launch System," presented at the LDIA, Aachen, 2015.
[4] L. Bertola, T. Cox, P. Wheeler, S. Garvey, H. Morvan, "Electromagnetic Launch Systems for Civil Aircraft Assisted Take-off," *Archive of Electrical Engineering,* vol. 64, pp. 543-554, 2015.
[5] G. Stumberger, D. Zarko, M. T. Aydemir, T. A. Lipo, "Design of a Linear Bulk Superconductor Magnet Synchronous Motor fo Electromagnetic Aircraft Launch Systems," *IEEE Transaction on Applied Superconductivity,* vol. 14, pp. 54-62, March 2004.
[6] J. X. Jin, L. H. Zheng, Y. G. Guo, J. G. Zhu, C. Grantham, C. C. Sorell, W. Xu, "High-Temperature Superconducting Linear Synchronous Motors Integrated with HTS Magnetic Levitation Components," *IEEE Transaction on Applied Superconductivity,* vol. 22, 2012.
[7] Columbus Superconductors Spa. (2014, October 2015). *Shape, dimensions and materials*. Available: http://www.columbussuperconductors.com/shape.asp
[8] S. Kusada, M. Igarashi, K. Nemoto, T. Okutomi, S. Hirano, K. Kuwano, T. Tominaga, M. Terai, T. Kuriyama, K. Tasaki, T. Tosaka, K. Marukawa, S. Hanai, T. Yamashita, Y. Yanase, H. Nakao, M. Yamaji "The Project Overview of the HTS Magnet for Superconducting Maglev," *IEEE Transaction on Applied Superconductivity,* vol. 17, pp. 2111-2116, 2007.
[9] X. Song, N. Mijatovic, B. B. Jensen, J. Holboll, "Design Study of Fully Superconducting Wind Turbine Generators," *IEEE Transaction on Applied Superconductivity,* vol. 25, 2015.
[10] C. Weng, M. Hu, H. Yu, T. Hong, H. Chen, R. Qu, H. Fang, "Design of a MgB$_2$ Supersucting Synchronous Generator," *25,* vol. 3, 2015.
[11] W. Goldacker, S. I. Schlachter, "HTS and MgB$_2$ cables for application in energy technology and magnets," Karlsruhe Institute of Technology2011.
[12] B. Backlund, M. Rahimo, S. Klaka, J. Siefken, "Topologies, voltage ratings and state of the art high power semiconductor devices for medium voltage wind energy conversion," presented at the Power Electronics and Machines in Wind Applications (PEMWA), Lincoln, NE, 2009.

[13] Z. Deng, I. Boldea, S. A. Nasar, "Fields in Permanent Magnet Linear Synchronous Machines," *IEEE Transaction on Magnetics,* vol. 2, pp. 107-112, 1986.

[14] M. Lyly, V. Lahtinen, A. Stenvall, L. Rostila, R. Mikkonen, "A Time-Harmonic Approach to Numerically Model Losses in the Metal Matrix in Twisted Superconductors in External Magnetic Field," *IEEE Transaction on Applied Superconductivity,* vol. 24, 2014.

[15] M. Arata, M. Kawai, T. Yamashita, M. Fujita T. Hamajim, Y. Sanada, A. Mtijra, M. Yamaguchi, M. Terai, S. Inadama, "Eddy Current Loss Reduction of Superconducting Magnets for MAGLEV with a Multilayer Superconducting Sheet," *IEEE Transaction on Applied Superconductivity,* vol. 7, pp. 912-915, 1997.

[16] W. J. Carr, *AC loss and Macroscopic Theory of Superconductors*: CRC Press, 2001.

[17] R. S. Weaver, "The Inductance of a Helix of any Pitch," Saskatoon, Canada21 March 2011.

[18] National Bureau of Standards USA, "The Self and Mutual Inductances of Linear Conductors," ed. Washington, 1907.

[19] J. F. Gieras, Z. J. Piech, B. Z. Tomczuk, *Linear Synchronous Motors - Transportation and Automation Systems*: CRC Press, 2011.

[20] I. Boldea, *Linear Electric Machines, Drives, and MAGLEVs Handbook*: CRC Press, Taylor & Francis Group, 2013.

[21] F. Berg, J. Palmer, L. Bertola, P. Miller, G. Dodds, "Cryogenic system options for a superconducting aircraft propulsion system," *IOP Conference Series: Materials Science and Engineering,* vol. 101, 2015.

[22] H. Hub. (2016). *Heathrow Hub Proposal*. Available: http://www.heathrowhub.com/our-proposal.aspx

[23] T. Telegraph. (2015). *Heathrow vs Gatwick expansion plans: the debate for and against runways at London's two main airports*. Available: http://www.telegraph.co.uk/news/2016/03/16/heathrow-vs-gatwick-expansion-plans-the-debate-for-and-against-r/